Electrochimica Acta 210 (2016) 285–292

Contents lists available at ScienceDirect

Electrochimica Acta

journal homepage: www.elsevier.com/locate/electacta

Pd on carbon nanotubes-supported Ag for formate oxidation: The effect of Ag on anti-poisoning performance

Jianshe Wang[a,b,*], Changhai Liu[b,c], Andrew Lushington[b], Niancai Cheng[b], Mohammad Norouzi Banis[b], Adam Riese[b], Xueliang Sun[b,*]

[a] School of Chemical Engineering and Energy, Zhengzhou University, Zhengzhou, Henan Province, 450000, PR China
[b] Department of Mechanical and Materials Engineering, The University of Western Ontario, ON, N6A 5B9, Canada
[c] School of Materials Science & Engineering, Changzhou University, Changzhou, Jiangsu Province, 213164, PR China

ARTICLE INFO

Article history:
Received 21 November 2015
Received in revised form 9 May 2016
Accepted 9 May 2016
Available online 25 May 2016

Keywords:
Formate oxidation
Pd-on-Ag
atomic layer deposition
anti-poisoning performance

ABSTRACT

For improving the utilization and anti-poisoning performance of Pd catalysts for formate oxidation, atomic layer deposition (ALD) method was used to deposit Pd on carbon nanotubes (CNTs) and CNTs-supported Ag (Ag/CNTs). The structures of the as-prepared Pd/CNTs and Pd-on-Ag/CNTs catalysts were characterized using X-ray diffraction (XRD) and high resolution transmission electron microscopy (HRTEM). Electrochemical characterization and high-angle annular dark-field scanning TEM (HADDF-STEM) confirmed the Pd-on-Ag structure. Pd utilization, activity, and anti-poisoning performance for Pd/CNTs and Pd-on-Ag/CNTs catalysts were compared, indicating that the overall performances of the Pd-on-Ag catalysts are superior to those of Pd on CNTs without Ag. Particularly, the mass specific chronoamperometric current (I_{CA}) of the Pd-on-Ag/CNTs (171.8 mA mg_{Pd}^{-1}) is two times greater compared to that of Pd/CNTs (70.0 mA mg_{Pd}^{-1}). X-ray photoelectron spectroscopy (XPS) was used to explain the improved anti-poisoning performance from the aspect of electronic Pd-Ag interaction. The results in this paper demonstrated the need for rationally engineered supports for improving the anti-poisoning performance of Pd-based anode catalysts.

1. Introduction

In recent years, direct formate fuel cells (DFFCs) [1–6] have drawn increasing research interest due to the following advantages: (i) lower anode overpotential for formate oxidation in comparison with methanol or ethanol oxidation [5]; (ii) formate fuel can be obtained from CO_2 electro-reduction, making DFFCs renewable power sources [7,8]; (iii) cheap, non-Pt materials can be used as cathode catalysts [9–11]. Till now, researches pertaining to formate oxidation catalysis are limited, and the main catalysts are still Pt- and Pd-based ones [4,5]. To lower the usage of noble metals (Pt and Pd) in practical applications, it is necessary to design catalysts with higher Pt and/or Pd utilization, for example, by employing core/shell [12–14] structure or other advanced architectures (like Pt-on-Au) [15–17]. In designing such low-noble-metal catalysts, the catalytic performance might be simultaneously improved. For example, Pt-on-Au catalysts have demonstrated extremely high activity for methanol [16] and formic acid oxidation [15,17] with ultra-low Pt content. Since Au in Pt-on-Au catalysts is still relatively expensive, replacing Au by Ag is economically reasonable. Moreover, because Ag bears similar electronic features to Au, Pt-on-Ag and Pd-on-Ag might also exhibit excellent anti-poisoning performance arising from the weakened CO adsorption by Ag [10,18,19]. To date there has been no report on such a catalyst design for formate oxidation. Further, since Ag is usually formed as particles on carbonaceous supports, depositing Pt or Pd predominantly on the Ag rather than onto the carbonaceous support is still challenging and has not been reported.

Atomic layer deposition (ALD) technique, with its unique capabilities for facile and controllable atomic-level manipulation, has been successfully employed in Pt-based electrocatalyst fabrication [20–24]. The Pt amount, particle size, and deposition site can all be well controlled. In contrast, Pd-based electrocatalysts prepared using ALD technique have been seldom reported [25], especially for formate oxidation. Considering that (i) Pd is similar to Pt in catalytic property but superior to Pt in terms of cost and abundance [26], and that (ii) the Pd-on-Ag structure

* Corresponding author. Tel.:+ 519 661 2111x87759; fax: +519 661 3020.
E-mail addresses: wangjs07@zzu.edu.cn, angelchem@126.com (J. Wang), xsun@eng.uwo.ca (X. Sun).

http://dx.doi.org/10.1016/j.electacta.2016.05.074
0013-4686/

might exhibit excellent performance in terms of Pd utilization and anti-poisoning performance, we herein employed ALD method to deposit Pd on CNTs (carbon nanotubes) and on Ag/CNTs (CNTs-supported Ag), and successfully obtain Pd/CNTs and Pd-on-Ag/CNTs catalysts, respectively (see Scheme 1). The Pd-on-Ag/CNTs catalysts showed superior anti-poisoning performance and higher Pd utilization in comparison with Pd/CNTs, demonstrating that Ag is an excellent substrate for Pd catalysts for formate oxidation. Besides, by changing the ALD cycle number the Pd particles size can be changed. The effect of particle size has also been analyzed.

2. Experimental

2.1. Chemicals

Multi-walled carbon nanotubes (CNTs) were obtained from Shenzhen Nanotech Port Co., Ltd. and the average diameter of CNTs are 40 ~ 60 nm. Sodium oleate, potassium formate (HCOOK) and other reagents were of analytical purity and used without further purification.

2.2. Preparation of Ag particles supported on CNTs (Ag/CNTs)

The as-received CNTs (300 mg) were first ultrasonicated in HCl (1 M, 50 mL) for 1 h to dissolve possible metal residues, then filtered, washed, and dried to obtain purified CNTs. For deposition of Ag particles on CNTs, 210 mg of purified CNTs were dispersed in a beaker containing 253 mg sodium oleate and ultrasonicated for 30 min, and then aqueous solution containing 141 mg $AgNO_3$ was added dropwise under magnetic stirring to form silver oleate on CNTs. After filteration and aqueous washing, the as-obtained sample of ~510 mg was collected and dried at 100 °C. Then 300 mg as-prepared samples were heated in a tube at 550 °C for 5 min under N_2 protection to decompose the silver oleate. Finally 160 mg of Ag/CNTs was obtained with a theoretical Ag content of 30 wt. %.

2.3. Preparation of Pd_x/CNTs and Pd_x-on-Ag/CNTs through ALD

ALD was performed using an Arradiance (Gemstar-8) system. Palladium was deposited using alternating exposure of Pd(II) hexafluoroacetylacetonate ($Pd(hfac)_2$) and formalin, both obtained from Sigma Aldrich. Formalin consists of a 37% solution of formaldehyde in water containing 10–15% methanol to inhibit the formation of paraformaldehyde. $Pd(hfac)_2$ was held in a stainless steel bubbler maintained at 85 °C. Manifolds in the ALD reactor were held at 130 °C to prevent readsorption of $Pd(hfac)_2$ while the chamber was held at 200 °C. Ultrahigh purity nitrogen (99.999%) was used as a carrier gas at a mass flow rate of 30 sccm. The ALD timing sequences used for deposition was 1 s–25 s–0.5 s–25 s.

The thus prepared catalysts were denoted as Pd_x/CNTs and Pd_x-on-Ag/CNTs, where the x represents the number of ALD cycles. The Pd contents in Pd_2/CNTs, Pd_{10}/CNTs, Pd_{25}/CNTs, Pd_2-on-Ag/CNTs, Pd_{10}-on-Ag/CNTs and Pd_{25}-on-Ag/CNTs were determined using inductively coupled plasma (ICP) emission spectrometer to be 0.12 wt. %, 0.44 wt. %, 2.45 wt. %, 0.24 wt. %, 0.67 wt. % and 2.94 wt. %, respectively.

2.4. Physical characterization of Pd_x/CNTs and Pd_x-on-Ag/CNTs

The X-ray diffraction (XRD) patterns of CNTs, Ag/CNTs, Pd_x/CNTs and Pd_x-on-Ag/GNs were recorded on a Bruker D8 Advance X-ray diffractometer using Cu-Ká as the radiation source.

The morphology of the catalysts was examined with transmission electron microscopy (TEM, FEI Quanta FRG 200F) operating at 200 kV and high-angle annular dark-field scanning TEM (HADDF-STEM).

The electronic structures of the catalysts were characterized with the X-ray photoelectron spectroscopy (XPS, Kratos Axis Yltra DLD, monochromatic Al Kα) in ultrahigh vacuum.

2.5. Electrochemical characterization of Pd_x/CNTs and Pd_x-on-Ag/CNTs

Catalyst inks were first prepared for coating on a glassy carbon (GC, Φ = 5 mm) electrode. Specifically, 2 mg Pd/CNTs (or Pd-on-Ag/CNTs) was mixed with 600 uL ethanol containing 0.4 mg Nafion® and ultrasonicated for 30 min to form homogeneous ink, then 15 μL ink was pipetted onto the GC electrode and dried using an infrared lamp. The theoretical mass loading of each catalyst is 0.05 mg on GC electrode.

A three-electrode cell coupled with an Autolab potentiostat/galvanostat (Model PGSTAT-30, Ecochemie, Brinkman Instrument) was used. A GC electrode, a Pt wire electrode and a Hg/HgO electrode were used as working electrode, counter electrode and reference electrode, respectively. All potentials herein were referred to Hg/HgO electrode, and all the electrochemical experiments were conducted at 25 °C in a N_2-saturated solution.

For each catalyst characterization, cyclic voltammetry (CV) was first conducted at 50 mV s^{-1} in 1 M KOH solution until stable cyclic voltammograms (CVs) were obtained. Then CVs for formate oxidation were recorded in 1 M KOH + 1 M HCOOK solution,

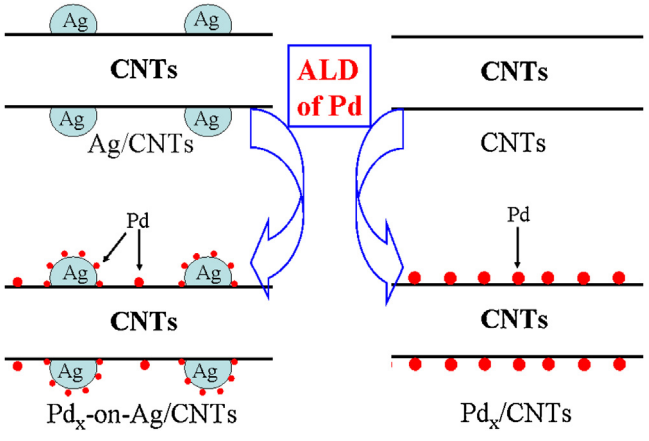

Scheme 1. Illustration of Pd deposition by ALD and the corresponding structure of Pd-on-Ag/CNTs versus Pd/CNTs.

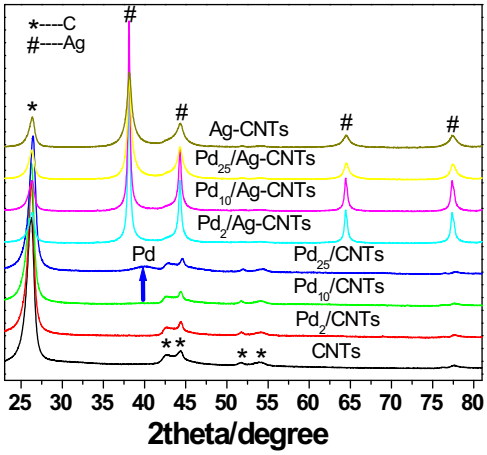

Fig 1. XRD patterns of CNTs, Pd_x/CNTs, Ag/CNTs and Pd_x-on-Ag/CNTs.

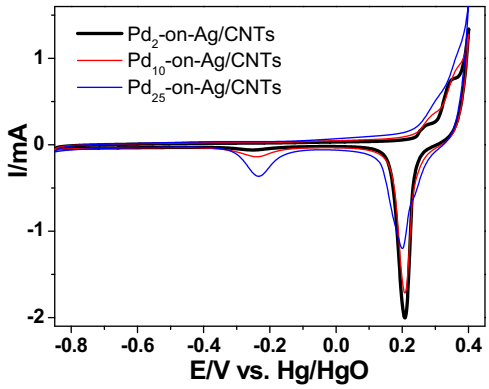

Fig. 2. CVs for Pd_x-on-Ag/CNTs recorded in 1 M KOH solution.

followed by corresponding chronoamperometry (CA) tests conducted at −0.4 V for 3000 s.

For CO stripping experiments, gaseous CO was bubbled into the electrolyte (1 M KOH) for 30 min to allow CO adsorption onto the electro-catalysts while maintaining a constant voltage of −0.8 V. Excess CO was purged out with N_2 for 20 min. Then two successive CVs for CO stripping were recorded at a scan rate of 20 mV s^{-1}.

3. Results and Discussion

3.1. Structural characterization for Pd_x/CNTs and Pd_x-on-Ag/CNTs

Fig. 1 outlines the XRD patterns obtained for Pd_x/CNTs and Pd_x-on-Ag/GNs as well as CNTs and Ag/CNTs as reference. The peak at 26.4° for all the XRD patterns can be ascribed to carbon (002) plane, indicating the graphitic structure of CNTs. When comparing the XRD patterns of Pd_{25}/CNTs and CNTs, we notice a new peak at ~40° that can be ascribed to Pd(111) [10]. This peak is weak with broad width indicating that the Pd content is low and the grain size is small. In contrast, no peak for Pd can be discerned for the XRD patterns of Pd_2/CNTs and Pd_{10}/CNTs, indicating that the Pd content is too low. For the XRD patterns of Ag/CNTs, four peaks at 38.1°, 44.2°, 64.4° and 77.4° can be ascribed to Ag(111), Ag(200), Ag(220) and Ag(311) [10,27], respectively, confirming the presence of metallic Ag in Ag/CNTs. As for the XRD patterns of Pd_x-on-Ag/CNTs, no Pd signal can be determined even though the Pd content of Pd_{25}-on-Ag/CNTs is slightly higher than that of Pd_{25}/CNTs (see the ICP results). This indicates that the Pd grain size in Pd_{25}-on-Ag/CNTs is too small (see the following analysis) to show detectible signal.

To confirm the existence of Pd moieties in Pd_x-on-Ag/CNTs, CVs were recorded for Pd_x-on-Ag/CNTs in 1 M KOH solution (see Fig. 2).

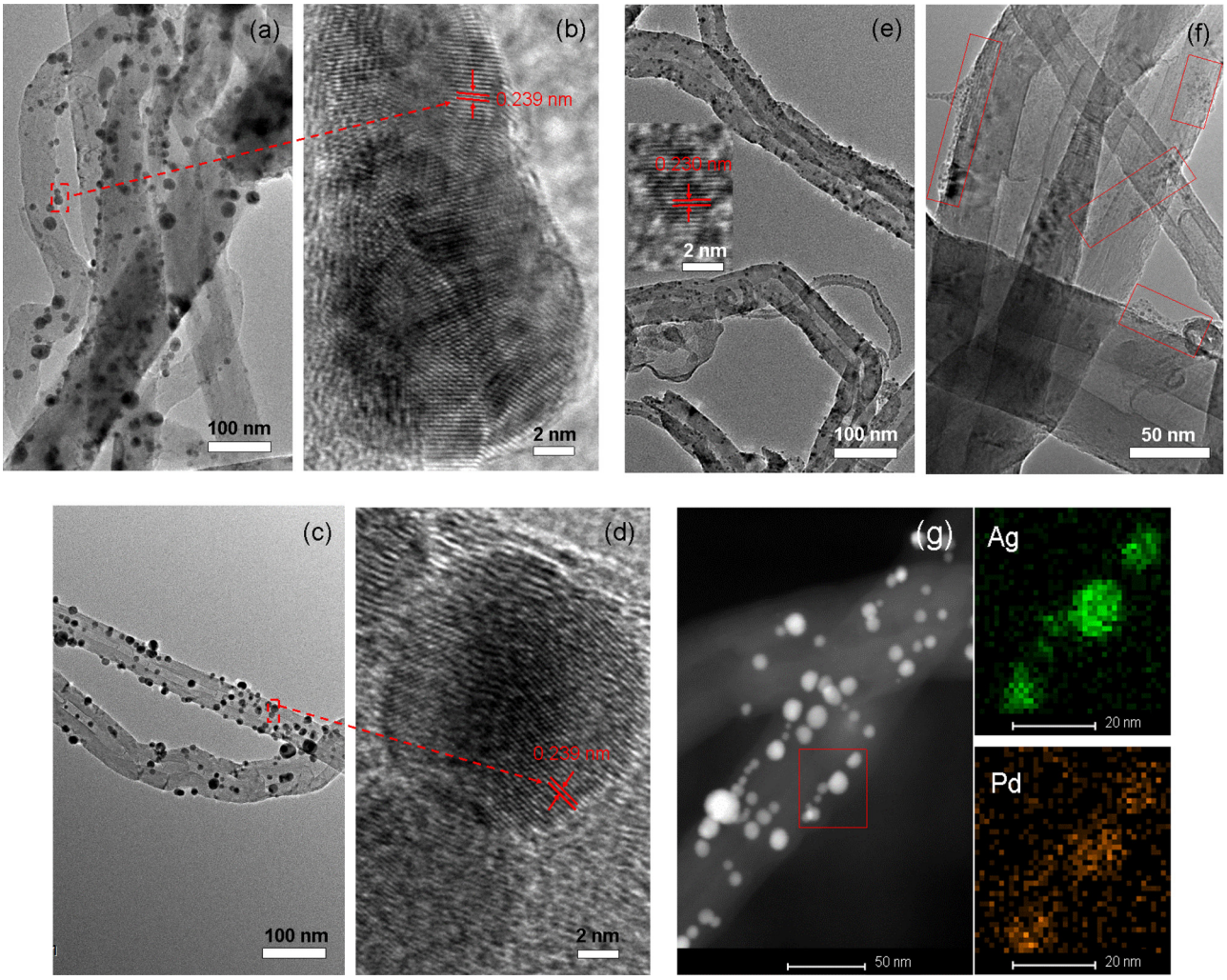

Fig. 3. (a) HRTEM image and (b) magnified micrographs of Ag/CNTs. (c) HRTEM image and (d) magnified micrographs of Pd_{25}-on-Ag/CNTs. (e) HRTEM image of Pd_{25}/CNTs. (f) HRTEM image of Pd_2/CNTs. (g) STEM image and corresponding EDS mapping of Pd_{25}-on-Ag/CNTs.

The cathodic peaks at ~0.2 V can be ascribed to the reduction of Ag oxide and the peaks at ~−0.24 V can be ascribed to the reduction of Pd oxide. It can be seen that, with increasing number of Pd ALD cycles, the peak intensity for Ag oxide reduction continually decreases while that for Pd oxide reduction repetitively increases, indicating that the Ag surface is gradually covered by Pd moieties to form the Pd-on-Ag structure.

To further confirm the fine structure of Pd_x-on-Ag/CNTs, high resolution TEM (HRTEM) were employed. The HRTEM images of Ag/CNTs are shown in Fig. 3(a) and (b) for reference. The HRTEM images of Pd_{25}-on-Ag/CNTs are shown in Fig. 3(c) and 3(d) while those of Pd_{25}/CNTs and Pd_2/CNTs are shown in Fig. 3(e) and (f), respectively. From Fig. 3(a) we can statistically determine the Ag particles size to be in the range of 5 ~ 11 nm. The magnified observation of a selected Ag particle confirmed a lattice distance of 0.239 nm corresponding to Ag(111) [28]. For Pd_{25}-on-Ag/CNTs in Fig. 3(c), the particle size distribution is similar to that in Fig. 3(a). The calculation of lattice distance in Fig. 3(d) confirmed the existence of metallic Ag, meaning that the Pd moieties cannot be clearly observed. This may be due to the super-small grain size of Pd moieties since the existence of Pd-on-Ag structure has been confirmed by the electrochemical results in Fig. 2. For the HRTEM image of Pd_{25}/CNTs in Fig. 3(e), a Pd particle of ~3 nm was observed to calculate the lattice distance (~0.230 nm). Bearing in mind that the Pd content of Pd_{25}/CNTs is similar to that of Pd_{25}-on-Ag/CNTs but the Pd existence in Pd_{25}-on-Ag/CNTs cannot be observed by HRTEM, we further assume that the Pd grains be smaller in the Pd_{25}-on-Ag structure. The HRTEM image of Pd_2/CNTs in 3(f) demonstrated that the average size of Pd particles in Pd_2/CNTs is evidently smaller than that for Pd_{25}/CNTs, and the distribution of

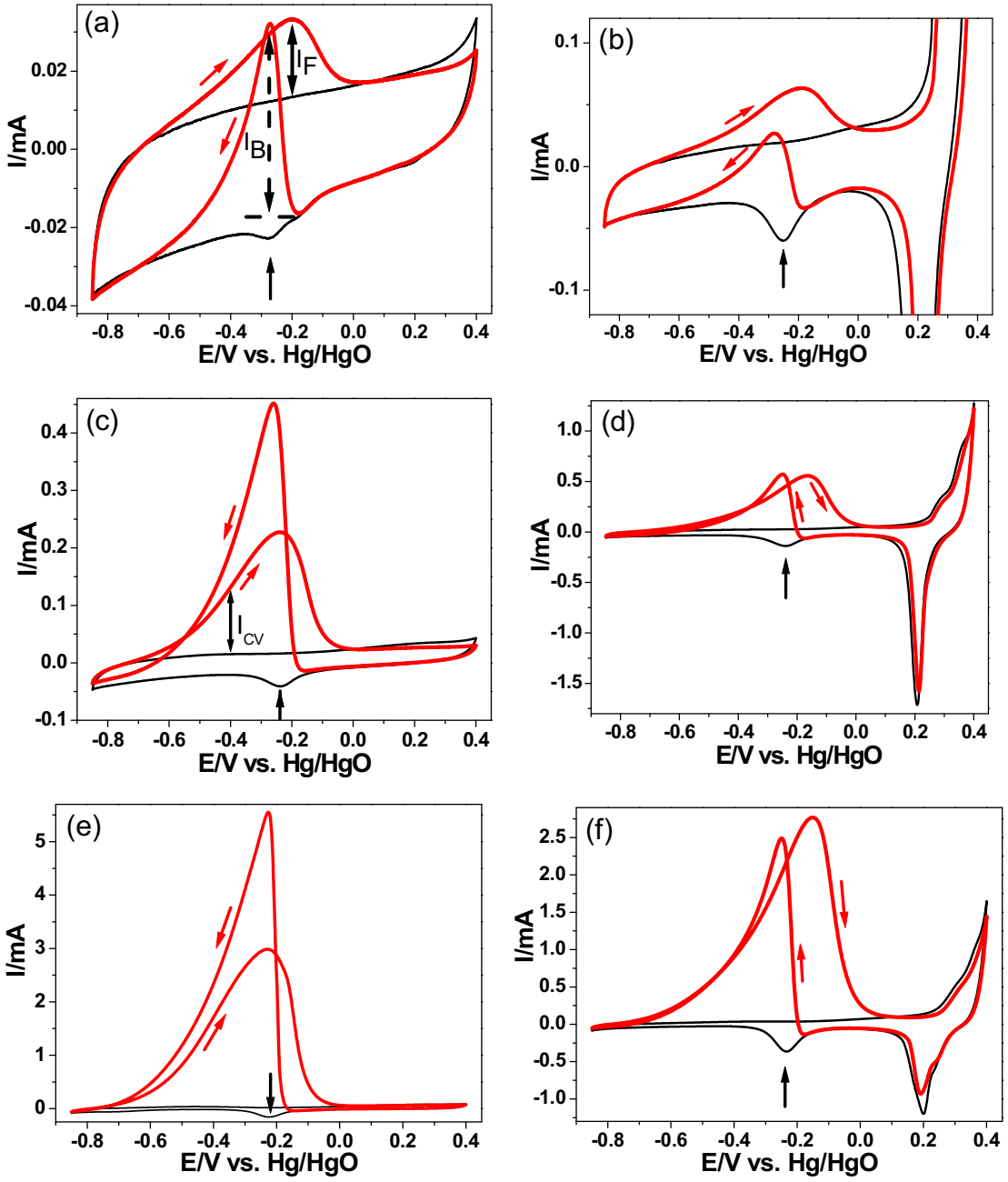

Fig. 4. CVs recorded at 50 mV s^{-1} in 1 M KOH + 1 M HCOOK for (a) Pd_2/CNTs, (b) Pd_2-on-Ag/CNTs, (c) Pd_{10}/CNTs, (d) Pd_{10}-on-Ag/CNTs, (e) Pd_{25}/CNTs and (f) Pd_{25}-on-Ag/CNTs. The black lines represent the corresponding CVs recorded in 1 M KOH at 50 mV s^{-1}.

Table 1
EAS, mass specific EAS, mass specific activity and area specific activity obtained from CVs in Fig. 4. (For interpretation of the references to colour in this table, the reader is referred to the web version of this article.)

	EAS/cm^2	EAS_m/cm^2 mg_{Pd}^{-1}	I_B/mA	I_m/mA mg_{Pd}^{-1}	I_A/mA cm^{-2}
Pd_2/CNTs	0.05	2083	0.0486	2025	0.97
Pd_{10}/CNTs	0.17	1875	0.465	5284	2.82
Pd_{25}/CNTs	0.91	1849	5.59	11408	6.18
Pd_2/Ag-CNTs	0.24	5000	0.0602	1254	0.25
Pd_{10}/Ag-CNTs	0.69	5149	0.632	4716	0.92
Pd_{25}/Ag-CNTs	1.71	2908	2.62	4456	1.53

Pd particles on CNTs was fairly inhomogeneous, as indicated by the red rectangles. This size difference can bring about noticeable effects on catalytic performance of Pd particles (see Section 3.2). Additionally, we used energy dispersive X-ray spectroscopy (EDS) coupled to STEM to verify the Pd-on-Ag structure of Pd_{25}-on-Ag/CNTs, as shown in Fig. 3(g). It can be seen that the signal of Pd moieties overlap consistently with the Ag signal, indicating that most of Pd moieties deposit on the surface of Ag particles to form the Pd-on-Ag structure.

3.2. Electrocatalytic performance of Pd_x/CNTs and Pd_x-on-Ag/CNTs

To compare the electrochemical performance of Pd_x/CNTs and Pd_x-on-Ag/CNTs, stable CVs were obtained in 1 M KOH and 1 M KOH + 1 M HCOOK solution, respectively, as shown in Fig. 4. The CVs recorded in 1 M KOH were used to obtain the net forward scanning current (I_F) and backward scanning current (I_B) of formate oxidation by comparing with CVs in 1 M KOH + 1 M HCOOK solution, as exemplified in Fig. 4(a). From Fig. 4(a) we can see that the Pd oxide reduction peak (see the solid black arrows) appears at a potential (-0.19 V) similar to that for the backward scanning peak in 1 M KOH + 1 M HCOOK solution. Herein this backward scanning peak might be ascribed to the oxidation of formate, rather than that of the poisoning species (like CO_{ad}) because there is no possibility of CO_{ad} formation when the Pd surface is composed of oxide within the high potential range [29]. Considering this assumption, the backward scanning current (I_B) can be accepted as a reflection of the true activity of Pd_2/CNTs for formate oxidation without the suppression of CO_{ad}. Furthermore, the I_B can also be used to calculate the mass activity (I_m) and area activity (I_A). Before calculating the I_A, the peak area for Pd oxide reduction was first integrated to obtain the electrochemical active surface (EAS) area using a coefficient of 375 $\mu C\ cm_{Pd}^{-2}$ [30]. Following this procedure, the EAS (cm^2), mass specific EAS ($cm^2\ mg_{Pt}^{-1}$), I_B (mA), I_m ($mA\ mg_{Pt}^{-1}$), I_A ($mA\ cm^{-2}$) for the six catalysts were collected in Table 1.

From Table 1 we can see that the mass specific EAS (EAS_m) decreases with increasing ALD cycle number for Pd_x/CNTs or Pd_x-on-Ag/CNTs. This is because the size of Pd particles increases with ALD cycle number, as reflected from Fig. 3(e) and (f). It can also be seen that the EAS_m of Pd_x-on-Ag/CNTs are all larger than those of Pd_x/CNTs, indicating the higher dispersion and smaller grain size of Pd moieties for the former. Remarkably, we can see that the EAS_m of Pd_{25}-on-Ag/CNTs is even higher than that of Pd_2/CNTs, confirming the very small size and high dispersion of Pd moieties in Pd-on-Ag structure and explaining the failure to observe the Pd existence using HRTEM in Fig. 3(d).

From Table 1 we can also see that the I_A for Pd_x/CNTs (or Pd_x-on-Ag/CNTs) increases with increasing the ALD cycle number, as indicated by the red and blue arrows. This might be due to the size effect [31,32], namely, variation of specific activity resulting from the size increase of the Pd particle (or Pd grains). In fact, this size increase is also reflected in the variation in peak potential for Pd oxide reduction (see Fig. 4). In Fig. 4 the formate oxidation during the backward scanning happens on pure Pd surface obtained from the Pd oxide reduction. Accordingly, the peak potential for formate oxidation (E_B) on Pd_x/CNTs or Pd_x-on-Ag/CNTs and the peak potential for Pd oxide reduction (E_{PdOx}) should show similar changing trend due to the size increase. So the values of E_B and E_{PdOx} were both collected to reflect this size effect, as shown in Fig. 5. From Fig. 5 we can see that the values of E_B and E_{PdOx} for Pd_x/CNTs or Pd_x-on-Ag/CNTs simultaneously increase with increasing the ALD cycle number. This trend indicates that with increasing the ALD cycle number and Pd particles size, the binding of oxygen-containing species with Pd get weaker, and correspondingly, the potential for Pd oxide reduction shifts to higher potential [31,32], confirming the existence of size effect.

As analyzed above, the backward scanning current (I_B) in Fig. 4 can be viewed as a reflection of the true activity for formate oxidation without the suppression of CO_{ad}. In comparison with I_B, the forward scanning currents (I_F) for formate oxidation on Pd_x/CNTs are smaller. One reason for this is the adsorption of CO_{ad} onto the Pd surface during forward scanning, which could suppress formate oxidation. Therefore, the ratio of I_B to I_F (I_B/I_F) can be used to reflect the anti-poisoning performance of Pd_x/CNTs and Pd_x-on-Ag/CNTs, as listed in Table 2. It can be seen that the I_F/I_B ratio increases with increasing ALD cycle number for Pd_x/CNTs and Pd_x-on-Ag/CNTs, indicating enhanced anti-poisoning performance due to the increased size of Pd particles (or grains). To verify this judgment, we also measured the corresponding chronoamperometry currents (I_{CA}) at −0.4 V for Pd_{10}/CNTs, Pd_{25}/CNTs, Pd_{10}-on-Ag/CNTs and Pd_{25}-on-Ag/CNTs (see Fig. 6) and calculated the ratio of I_{CA} to I_{CV}, where the I_{CV} presents the dynamic currents obtained from the CVs at −0.4 V, as exemplified in Fig. 4(c). The results are

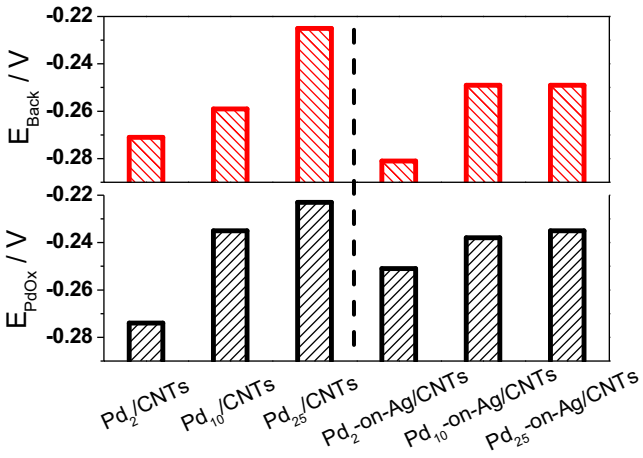

Fig. 5. the changing trend of the peak potentials for formate oxidation and Pd oxide reduction with increasing ALD cycle number.

Table 2
Analysis of the anti-poisoning performances of Pd_x/CNTs and Pd_x-on-Ag/CNTs based upon the results in Fig. 4. (For interpretation of the references to colour in this table, the reader is referred to the web version of this article.)

	I_F/mA	I_B/mA	I_F/I_B/%	I_{CA}/mA	I_{CV}/mA	I_{CA}/I_{CV}/%
Pd_2/CNTs	0.0199	0.0486	40.9	-	-	-
Pd_{10}/CNTs	0.211	0.465	45.4	0.00189	0.115	1.63
Pd_{25}/CNTs	2.97	5.59	53.1	0.0343	1.670	2.05
Pd_2/Ag-CNTs	0.0420	0.0602	69.8	-	-	-
Pd_{10}/Ag-CNTs	0.527	0.632	83.4	0.0109	0.171	6.37
Pd_{25}/Ag-CNTs	2.73	2.62	104	0.101	0.859	11.8

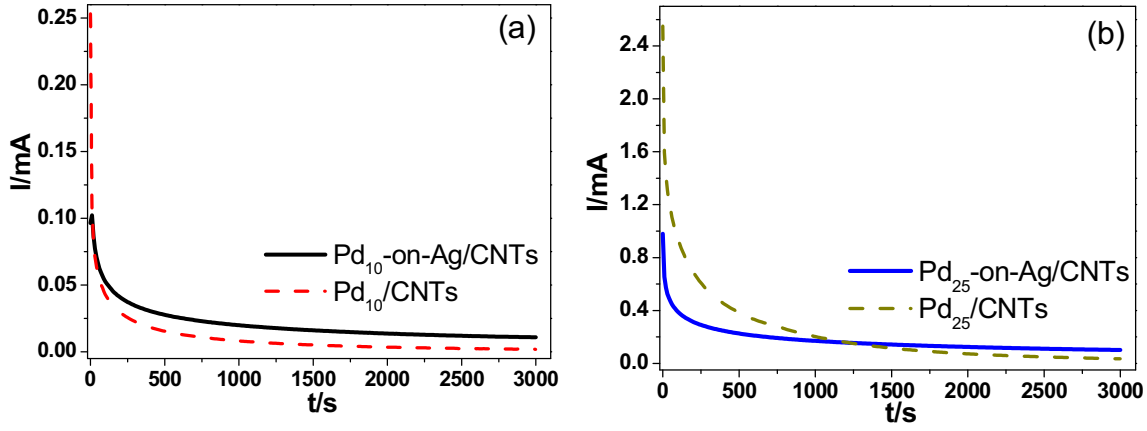

Fig. 6. CA curves for (a) Pd_{10}/CNTs and Pd_{10}-on-Ag/CNTs and (b) Pd_{25}/CNTs and Pd_{25}-on-Ag/CNTs recorded at −0.4 V in 1 M KOH + 1 M HCOOK solution.

shown in Table 2. Comparing the values of I_{CA}/I_{CV} for Pd_{10}/CNTs versus Pd_{25}/CNTs (or Pd_{10}-on-Ag/CNTs versus Pd_{25}-on-Ag/CNTs), we can see that they all increase with increasing the ALD cycle number, confirming the better anti-poisoning performance for larger Pd particles (or grains) due to the size effect. The size effect can be explained from the aspect of the increasing adsorption strength of various species like CO and oxygen-containing species on surface of smaller Pd entities.

From the EAS_m in Table 1, we know that the dispersion of Pd moieties on Ag substrate is higher than Pd on CNTs. From the results in Table 2, we know that Pd particles (or grains) with higher dispersion exhibit inferior anti-poisoning performance for Pd_x/CNTs or Pd_x-on-Ag/CNTs. However, for Pd_x-on-Ag/CNTs with higher Pd dispersion in comparison with Pd_x/CNTs (see EAS_m in Table 1), the corresponding anti-poisoning performances are all superior (see Table 2). The values of I_F/I_B and I_{CA}/I_{CV} for Pd_x-on-Ag/CNTs are all higher than the values for Pd_x/CNTs, indicating that the Ag substrate plays a positive role in improving the anti-poisoning performance of Pd catalysts. In fact, the superior anti-poison performance of Pd_x-on-Ag/CNTs to Pd_x/CNTs can be directly demonstrated from Fig. 6. Comparing Pd_{10}-on-Ag/CNTs with Pd_{10}/CNTs or Pd_{25}-on-Ag/CNTs with Pd_{25}/CNTs, the final currents for the catalyst supported by Ag/CNT are all higher than those supported by CNTs alone, although the initial currents are evidently higher for the latter.

Based upon the CA currents (I_{CA}) obtained from Fig. 6, the mass specific I_{CA} were further calculated for Pd_{10}/CNTs (21.5 mA mg_{Pd}^{-1}), Pd_{25}/CNTs (70.0 mA mg_{Pd}^{-1}), Pd_{10}-on-Ag/CNTs (81.3 mA mg_{Pd}^{-1}) and Pd_{25}-on-Ag/CNTs (171.8 mA mg_{Pd}^{-1}). The results indicate that the Pd_x-on-Ag/CNTs are superior to Pd_x/CNTs, confirming the important role of Ag substrate in upgrading the anti-poisoning performance of Pd. On the other hand, judging from the mass specific CV currents (I_m) (see Table 1), Pd_x/CNTs seems superior to the counterpart of Pd_x-on-Ag/CNTs. This can be explained from the aspect of size effect. Namely, the Pd in Pd_x-on-Ag/CNTs is far more dispersed, resulting in lower specific activity. It is noteworthy that, when comparing Pd_{25}-on-Ag/CNTs with Pd_{10}/CNTs, we found that the I_m of the former is nearly 2.2 times that of the latter, although the EAS_m of the former is nearly 1.4 times that of the latter and thus the size effect is unfavorable for the former. This result indicated that the Ag substrate undoubtedly posed a positive effect on the activity of Pd moieties. Considering above results, it is advisable to use the CA currents (I_{CA}), rather than CV currents as the evaluation index of catalysts performance because the CA currents are more representative of the operation for a real DFFC.

3.3. Mechanism analysis for the improved anti-poisoning performance of Pd_x-on-Ag/CNTs

To understand the role of Ag in upgrading the anti-poisoning performance of Pd moieties, CO stripping tests were conducted on Pd_{25}/CNTs and Pd_{10}-on-Ag/CNTs, as shown in Fig. 7. It can be seen that the onset potential (or peak potential) for CO stripping on Pd_{10}-on-Ag/CNTs is lower than those for Pd_{25}/CNTs, indicating that the CO species adsorb more weakly on Pd-on-Ag/CNTs than on Pd/CNTs. More interestingly, although the peak area of Pd oxide reduction for Pd_{10}-on-Ag/CNTs and Pd_{25}/CNTs is not largely different, the corresponding H region profile for the former is quite inconspicuous in comparison with the latter. Specifically, hydrogen adsorption features can hardly be observed on Pd_{10}-on-Ag/CNTs, indicating weak affinity of H adsorption on Pd-on-Ag. Herein we noticed that the strength of CO and H adsorption on Pd-on-Ag are simultaneously weaker in comparison with the case on Pd/CNTs. The reason might be ascribed to the electronic effect modulated by Ag substrate (see the XPS analysis). In fact, besides weakening the CO and H adsorption, Ag substrate also affects the

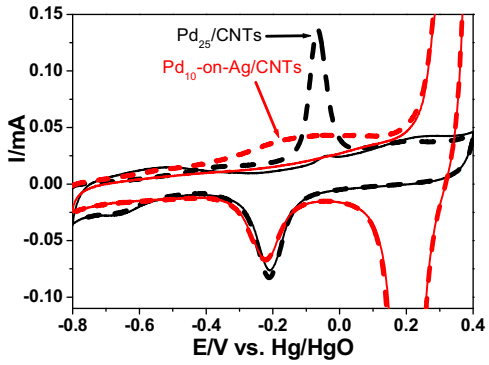

Fig. 7. Curves for CO stripping on Pd_{25}/CNTs and Pd_{10}-on-Ag/GNs recorded at 20 mV s^{-1} in 1 M KOH.

Pd oxide reduction behavior (see Fig. 5). As above analyzed for E_{PdOx} in Fig. 5, the binding of oxygen-containing species with Pd get stronger with increasing Pd dispersion in Pd_x/CNTs or Pd_x-on-Ag/CNTs (size effect). Because the Pd dispersion in Pd_x-on-Ag/CNTs is higher in comparison with Pd_2/CNTs (judging from the EAS_m in Table 1), the adsorption of oxygen-containing species on Pd surface of Pd_x-on-Ag/CNTs should be stronger, and correspondingly the E_{PdOx} values for Pd_x-on-Ag/CNTs should be lower than that for Pd_2/CNTs. However, the E_{PdOx} values for Pd_x-on-Ag/CNTs are all higher than that for Pd_2/CNTs (−0.274 V, see Fig. 5), indicating that the binding of the oxygen-containing species with Pd in Pd_x-on-Ag/CNTs is weakened, which can be ascribed to the Ag substrate.

To understand the possible reason for the weakened adsorption of CO, H, and oxygen-containing species on Pd surface due to Ag substrate, XPS data was collected on Pd_{25}/CNTs and Pd_{25}-on-Ag/CNTs and the Pd 3d spectra were deconvoluted into two pairs of doublets, as shown in Fig. 8. The more intense doublet (at 335.2 and 340.5 eV for Pd_{25}-on-Ag/CNTs, 335.7 and 341.1 eV for Pd_{25}/CNTs) could be assigned to Pd at zero valence state, while the weaker doublet with binding energies higher than those of zero valence corresponded to Pd at oxidized state. It can be seen that the binding energy of Pd $3d_{5/2}$ and $3d_{3/2}$ for Pd_{25}-on-Ag/CNTs shifted to lower values compared with Pd_{25}/CNTs. Furthermore, the proportion of oxidized Pd decreased from 47.4% for Pd_{25}/CNTs to 39.8% for Pd_{25}-on-Ag/CNTs, in agreement with above judgment that the adsorption of oxygen-containing species with Pd in Pd_x-on-Ag/CNTs is weakened. The above results can be attributed to the electronic interactions between Pd and Ag. In fact, similar phenomena of a negative shift in BE have been observed in Ag-Pd [33], Ag-Pt [34] and Au-Pd [35] catalysts. According to the study of Liu et al., Ag will donate some electrons to Pd, as can be reflected from the decreasing intensity of white-line in synchrotron radiation characterization [33]. Accordingly, the Fermi level will

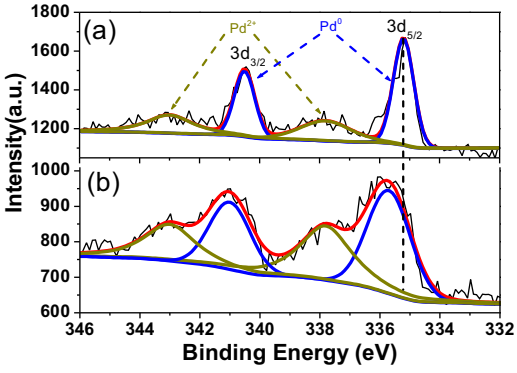

Fig. 8. XPS spectra in the Pd_{3d} region for (a) Pd_{25}-on-Ag/CNTs and (b) Pd_{25}/CNTs.

increase relatively, which will weaken the adsorption of certain species (including CO, H and oxygen-containing species) on Pd surface. For formate oxidation on Pd_x-on-Ag/CNTs versus Pd_x/CNTs, the weakened CO adsorption on the former would then translate to improved anti-poisoning performance.

4. Conclusion

Using ALD, Pd was deposited on Ag/CNTs and CNTs to form Pd_x-on-Ag/CNTs and Pd_x/CNTs as catalysts for formate oxidation. The anti-poisoning performances of the former catalysts were superior to those of the latter. The reason for this can be ascribed to the electronic effect of Ag substrate. On the other hand, the corresponding mass specific activities of the former, at first sight, seem lower than those of the latter due to the size effect. This superficial disagreement reflects the necessity of evaluating catalyst performance preferentially based upon the CA results. In conclusion, the present work showed that the substrate materials are critical for improving the anti-poisoning performance of Pd catalysts.

Acknowledgments

This research is financially supported by the National Natural Science Foundation of China (U1304215) and the China Scholarship Council (201308410311). This research was also supported by Natural Sciences and Engineering Research Council of Canada (NSERC), Canada Research Chair (CRC) Program, Canada Foundation for Innovation (CFI), and the University of Western Ontario.

References

[1] J.H. Jiang, A. Wieckowski, Prospective direct formate fuel cell, Electrochem. Commun. 18 (2012) 41.
[2] A.M. Bartrom, J. Ta, T.Q. Nguyen, J. Her, A. Donovan, J.L. Haan, Optimization of an anode fabrication method for the alkaline Direct Formate Fuel Cell, J. Power Sources. 229 (2013) 234.
[3] J.H. Jiang, J. Scott, A. Wieckowski, Direct evidence of a triple-path mechanism of formate electrooxidation on Pt black in alkaline media at varying temperature Part I: The electrochemical studies, Electrochimi. Acta. 104 (2013) 124.
[4] J. John, H.S. Wang, E.D. Rus, H.D. Abruna, Mechanistic studies of formate oxidation on platinum in alkaline medium, J. Phys. Chem. C. 116 (2012) 5810.
[5] J. Noborikawa, J. Lau, J. Ta, S.Z. Hu, L. Scudiero, S. Derakhshan, S. Ha, J.L. Haan, Palladium-copper electrocatalyst for promotion of oxidation of formate and ethanol in alkaline media, Electrochimi. Acta. 137 (2014) 654.
[6] L. Zeng, Z.K. Tang, T.S. Zhao, A high-performance alkaline exchange membrane direct formate fuel cell, Appl. Energy. 115 (2014) 405.
[7] S. Zhang, P. Kang, T.J. Meyer, Nanostructured tin catalysts for selective electrochemical reduction of carbon dioxide to formate, J. Am. Chem. Soc. 136 (2014) 1734.
[8] S. Zhang, P. Kang, S. Ubnoske, M.K. Brennaman, N. Song, R.L. House, J.T. Glass, T. J. Meyer, Polyethylenimine-enhanced electrocatalytic reduction of CO_2 to formate at nitrogen-doped carbon nanomaterials, J. Am. Chem. Soc. 136 (2014) 7845.
[9] H.Y. Zhu, S. Zhang, Y.X. Huang, L.H. Wu, S.H. Sun, Monodisperse $M_xFe_{3-x}O_4$ (M = Fe Cu, Co, Mn) nanoparticles and their electrocatalysis for oxygen reduction reaction, Nano Lett. 13 (2013) 2947.
[10] D.A. Slanac, W.G. Hardin, K.P. Johnston, K.J. Stevenson, Atomic ensemble and electronic effects in Ag-rich AgPd nanoalloy catalysts for oxygen reduction in alkaline media, J. Am. Chem. Soc. 134 (2012) 9812.
[11] D.S. Geng, Y. Chen, Y.G. Chen, Y.L. Li, R.Y. Li, X.L. Sun, S.Y. Ye, S. Knights, High oxygen-reduction activity and durability of nitrogen-doped grapheme, Energy Environ. Sci. 4 (2011) 760.
[12] D. Dang, S.J. Liao, F. Luo, S.Y. Hou, H.Y. Song, P.Y. Huang, A pulse electrochemical deposition method to prepare membrane electrode assemblies with ultra-low anode Pt loadings through in situ construction of active core-shell nanoparticles on an electrode, J. Power Sources. 260 (2014) 27.
[13] M.J. Weber, A.J.M. Mackus, M.A. Verheijen, C. van der Marel, W.M.M. Kessels, Supported core/shell bimetallic nanoparticles synthesis by atomic layer deposition, Chem. Mater. 24 (2012) 2793.
[14] Y. Zhang, Y.C. Hsieh, V. Volkov, D. Su, W. An, R. Si, Y.M. Zhu, P. Liu, J.X. Wang, R.R. Adzic, High performance Pt monolayer catalysts produced via core-catalyzed coating in ethanol, ACS Catal. 4 (2014) 738.
[15] S. Yang, H. Lee, Atomically dispersed platinum on gold nano-octahedra with high catalytic activity on formic acid oxidation, ACS Catal. 3 (2013) 437.

[16] J.S. Wang, R.R. Shi, X. Guo, J.Y. Xi, J.H. Zhao, C.Y. Song, L.C. Wang, J.J. Zhang, Highly active Pt-on-Au catalysts for methanol oxidation in alkaline media involving a synergistic interaction between Pt and Au, Electrochimi. Acta. 123 (2014) 309.
[17] G.R. Zhang, D. Zhao, Y.Y. Feng, B.S. Zhang, D.S. Su, G. Liu, B.Q. Xu, Catalytic Pt-on-Au nanostructures: why Pt becomes more active on smaller Au particles, ACS Nano. 6 (2012) 2226.
[18] S.T. Nguyen, H.M. Law, H.T. Nguyen, N. Kristian, S.Y. Wang, S.H. Chan, X. Wang, Enhancement effect of Ag for Pd/C towards the ethanol electro-oxidation in alkaline media, Appl. Catal. B-Environ. 91 (2009) 507.
[19] C. Wen, A.Y. Yin, W.L. Dai, Recent advances in silver-based heterogeneous catalysts for green chemistry processes, Appl. Catal. B-Environ. 160 (2014) 730.
[20] B.J. O'Neill, D.H.K. Jackson, J. Lee, C. Canlas, P.C. Stair, C.L. Marshall, J.W. Elam, T. F. Kuech, J.A. Dumesic, G.W. Huber, Catalyst design with atomic layer deposition, ACS Catal. 5 (2015) 1804.
[21] S.H. Sun, G.X. Zhang, N. Gauquelin, N. Chen, J.G. Zhou, S.L. Yang, W.F. Chen, X.B. Meng, D.S. Geng, M.N. Banis, R.Y. Li, S.Y. Ye, S. Knights, G.A. Botton, T.K. Sham, X. L. Sun, Single-atom catalysis using Pt/graphene achieved through atomic layer deposition, Sci. Rep. 3 (2013) 1775.
[22] N.C. Cheng, M.N. Banis, J. Liu, A. Riese, X. Li, R.Y. Li, S.Y. Ye, S. Knights, X.L. Sun, Extremely stable platinum nanoparticles encapsulated in zirconia nanocages by area-selective atomic layer deposition for oxygen reduction reaction, Adv. Mater. 27 (2015) 277.
[23] L. Assaud, J. Schumacher, A. Tafel, S. Bochmann, S. Christiansen, J. Bachmann, Systematic increase of electrocatalytic turnover at nanoporous platinum surfaces prepared by atomic layer deposition, J. Mater. Chem. A. 3 (2015) 8450.
[24] R.S. Juang, C.T. Hsieh, J.Q. Hsiao, H.T. Hsiao, D.Y. Tzou, M.M. Huq, Size-controlled platinum nanoparticles prepared by modified-version atomic layer deposition for ethanol oxidation, J. Power Sources. 275 (2015) 845.
[25] E. Rikkinen, A. Santasalo-Aarnio, S. Airaksinen, M. Borghei, V. Viitanen, J. Sainio, E.I. Kauppinen, T. Kallio, A.O.I. Krause, Atomic layer deposition preparation of Pd nanoparticles on a porous carbon support for alcohol oxidation, J. Phys. Chem. C. 115 (2011) 23067.
[26] E. Antolini, Palladium in fuel cell catalysis, Energy Environ. Sci. 2 (2009) 915.
[27] G.L. Li, L.H. Jiang, Q. Jiang, S.L. Wang, G.Q. Sun, Preparation and characterization of Pd_xAg_y/C electrocatalysts for ethanol electrooxidation reaction in alkaline media, Electrochimi. Acta. 56 (2011) 7703.
[28] Y.Z. Lu, W. Chen, Nanoneedle-covered Pd-Ag nanotubes: high electrocatalytic activity for formic acid oxidation, J. Phys. Chem. C. 114 (2010) 21190.
[29] A.M. Hofstead-Duffy, D.J. Chen, S.G. Sun, Y.Y.J. Tong, Origin of the current peak of negative scan in the cyclic voltammetry of methanol electro-oxidation on Pt-based electrocatalysts: a revisit to the current ratio criterion, J. Mater. Chem. 22 (2012) 5205.
[30] S. Henning, J. Herranz, H.A. Gasteiger, Bulk-palladium and palladium-on-gold electrocatalysts for the oxidation of hydrogen in alkaline electrolyte, J. Electrochem. Soc. 162 (2015) F178.
[31] A. Anastasopoulos, J.C. Davies, L. Hannah, B.E. Hayden, C.E. Lee, C. Milhano, C. Mormiche, L. Offin, The particle size dependence of the oxygen reduction reaction for carbon-supported platinum and palladium, ChemSusChem. 6 (2013) 1973.
[32] X.X. Li, X.P. Qiu, H.P. Yuan, L.Q. Chen, W.T. Zhu, Size-effect on the activity of anodic catalysts in alcohol and CO electrooxidation, J. Power Sources. 184 (2008) 353.
[33] C.H. Liu, X.Q. Chen, Y.F. Hu, T.K. Sham, Q.J. Sun, J.B. Chang, X. Gao, X.H. Sun, S.D. Wang, One-pot environmentally friendly approach toward highly catalytically active bimetal-nanoparticle-graphene hybrids, ACS Appl. Mater. Interfaces. 5 (2013) 5072.
[34] J.Y. Cao, M.W. Guo, J.Y. Wu, J. Xu, W.C. Wang, Z.D. Chen, Carbon-supported Ag@Pt core-shell nanoparticles with enhanced electrochemical activity for methanol oxidation and oxygen reduction reaction, J. Power Sources. 277 (2015) 155.
[35] H.W. Wang, C.L. Wang, H. Yan, H. Yi, J.L. Lu, Precisely-controlled synthesis of Au@Pd core-shell bimetallic catalyst via atomic layer deposition for selective oxidation of benzyl alcohol, J. Catal. 324 (2015) 59.